

Searching for High-Energy γ -Ray Counterparts to Gravitational Wave Sources with *Fermi*-LAT: a Needle in a Haystack

G. Vianello¹, N. Omodei¹, J. Chiang¹

ABSTRACT

At least a fraction of Gravitational Wave (GW) progenitors are expected to emit an electromagnetic (EM) signal in the form of a short gamma-ray burst (sGRB). The discovery of such a transient EM counterpart is challenging because the LIGO/VIRGO localization region is much larger (several hundreds of square degrees) than the field of view of X-ray, optical and radio telescopes. The *Fermi* Large Area Telescope (LAT) has a wide field of view (~ 2.4 sr), and detects $\sim 2 - 3$ sGRBs per year above 100 MeV. It can detect them not only during the short prompt phase, but also during their long-lasting high-energy afterglow phase. If other wide-field high-energy instruments such as *Fermi*-GBM, *Swift*-BAT or *INTEGRAL*-ISGRI cannot detect or localize with enough precision an EM counterpart during the prompt phase, the LAT can potentially pinpoint it with $\lesssim 10$ arcmin accuracy during the afterglow phase. This routinely happens with gamma-ray bursts. Moreover, the LAT will cover the entire localization region within hours of any triggers during normal operations, allowing upper limits to be evaluated. We illustrate two new ad hoc methods to search for EM counterparts with the LAT and to measure upper limits, and their application to the GW candidate LVT151012.

Subject headings: gravitational waves, gamma rays: general, methods: observational

¹W. W. Hansen Experimental Physics Laboratory, Kavli Institute for Particle Astrophysics and Cosmology, Department of Physics and SLAC National Accelerator Laboratory, Stanford University, Stanford, CA 94305, USA

1. Introduction

The first direct detection of a Gravitational Wave event (GW) by the recently upgraded LIGO (Abramovici et al. 1992; Abbott et al. 2009, 2016c) opened a new era in astronomy. The first science run ‘O1’ with the Advanced LIGO detector started in September 2015, and two high-significance events (GW150914 and GW151226) and one sub-threshold event (LVT151012) were reported (Abbott et al. 2016c,a). These three events were compatible with the signal expected from the merger of two Black Holes (BH). In future LIGO science runs, additional sources of GW events might include the mergers of other compact object binary systems: neutron star-black hole (NS-BH) and neutron star-neutron star (NS-NS).

The identification and study of electromagnetic counterparts (EM) to GW events is important for several reasons. It resolves degeneracies associated with the inferred binary parameters and allows for a cross-check between the distances measured through the GW signal with the redshifts measured through the EM counterpart, providing an independent constraint on cosmological models. The simultaneous detection of a clear EM counterpart can also confirm near-threshold or sub-threshold GW events, effectively increasing the sensitivity of the search and the distance to which GW events can be detected by LIGO/VIRGO. The potential wealth of complementary information encoded in the EM signal is likewise essential to fully unravel the astrophysical context of the event. However, the discovery of an EM counterpart is challenging because the localization regions of a GW event provided by LIGO/VIRGO are currently as large as several hundred of square degrees, much larger

than the field-of-view (FoV) of a typical X-ray, optical or radio telescopes (Abbott et al. 2016b). The luminosity of the expected EM counterpart is also expected to decay rapidly, leaving a short time window to complete the coverage of the localization region. On the other hand, hard X-ray telescopes such as *Swift*-BAT (Barthelmy et al. 2005) and *INTEGRAL*-ISGRI (Mereghetti et al. 2003), as well as γ -ray detectors such as the *Fermi* Gamma-Ray Burst Monitor (GBM, Meegan et al. 2009) *Fermi*/LAT (Atwood et al. 2009) and HAWC (Abeysekara et al. 2012), have much larger FoVs and can cover the localization region much more quickly. They are therefore expected to play a major role in the discovery of the first EM counterpart to a GW event.

Short gamma-ray bursts (sGRBs) are a class of GRB with a duration $\lesssim 2$ s, and they are thought to be associated with the mergers of BH-NS or NS-NS binaries (Eichler et al. 1989, Narayan et al. 1992, Lee & Ramirez-Ruiz 2007, and Nakar 2007). They are therefore the expected EM counterparts for GW events involving at least one NS. *Fermi*-GBM is the most prolific detector of sGRBs (~ 40 per year), and it is likely to be the first instrument to firmly detect an EM counterpart to a GW event (Connaughton et al. 2016). However, it localizes sGRBs with uncertainties of the order of a few degrees, making the follow-up by instruments at other wavelengths challenging. Coded-mask telescopes such as BAT and ISGRI can localize events with arcmin precision, but they have a smaller FoV and indeed detect ~ 8 sGRBs per year. HAWC has a very large FoV, but as yet has not detected its first GRB. The *Fermi* observatory was launched in June 2008 and orbits the Earth at an altitude of ~ 560 km with a period of 96.5 minutes. The *Fermi* Large Area Telescope (LAT) (Atwood et al. 2009) is a pair-conversion

telescope that detects γ rays in the energy range from 20 MeV to more than 300 GeV. It has a FoV of ~ 2.4 sr and it covers the entire sky every ~ 3 hours during normal operations. It detects around 15 gamma-ray bursts (GRB) per year, among them 2–3 are of the short-duration class, with localization of the order of ~ 10 arcmin (Vianello et al. 2015). When detected by the LAT at high energy (> 100 MeV), sGRBs have a substantially longer duration with respect to their keV-MeV emission. This long-lasting emission is thought to be related to the so-called afterglow emission, observed also at other wavelengths (De Pasquale et al. 2010; Ackermann et al. 2013; Kouveliotou et al. 2013). *Fermi*-LAT is the only wide-field instrument that has detected and localized a sGRB *during its afterglow phase* starting from the GBM localization. MASTER and iPTF have been able to do the same, but only for *long* GRBs so far Lipunov et al. (2016); Singer et al. (2015). Should the detection of an EM counterpart be made by the GBM, *Fermi*-LAT could reduce substantially the localization uncertainty, facilitating follow-up at other wavelengths. Should the counterpart be occulted by the Earth for the GBM, and outside the FoV of coded mask instruments, then the LAT would be the only instrument that could still detect the GRB in the 1–2 hours after the burst. Therefore, *Fermi*-LAT plays a unique role in facilitating the multi-wavelength follow-up of GW events. This happens routinely already for GRBs, as the vast majority of GRBs detected by the GBM that had a LAT localization, had also a successful follow up that led to the spectroscopic measurements of more than 20 redshifts (Vianello et al. 2015).

Very bright GRBs can also be localized by the LAT on-board with an accuracy between 0.1 and ~ 0.5 deg. This localization is then dis-

tributed within seconds to observatories on the ground, allowing for quick follow-up. This has so far happened 4 times in 8 years *Fermi* mission (Ohno & Pelassa 2009; Racusin et al. 2013; Longo et al. 2016; Dirirsa et al. 2016).

According to the standard model of GRBs the afterglow is expected to become less collimated than the prompt emission. In principle, therefore, *Fermi*-LAT could also detect “orphan” afterglows (Ghirlanda et al. 2015), i.e., afterglows of short GRBs whose emission was not observable by other wide-field instruments during the prompt phase because of the viewing geometry. However, no “orphan” GRB afterglow has been detected up to now and hence we see this scenario as unlikely.

BH-BH mergers are sources of GW, but are not expected to produce EM signals. *Fermi*-GBM observed a low-significance candidate counterpart 0.4 s after GW 150914, deemed GW 150914-GBM, with a chance coincidence probability of 0.2 percent (Connaughton et al. 2016) assuming a linear prior on the time separation from the GW event. Lyutikov (2016) contests this association on the grounds of the constraints it imposes on the circum-merger environment, while other authors argue against it mainly due to the non-detection by the *INTEGRAL*-ACS instrument (Greiner et al. 2016; Savchenko et al. 2016). The possible association between BH-BH mergers and γ -ray transients will be addressed by future GW events. If confirmed, it would constitute a surprise that would require new models, such as those published following the report of GW150914-GBM (e.g., Loeb 2016, Frascetti 2016, Janiuk et al. 2016, and Perna et al. 2016). Some of these new models foresee a counterpart similar to a standard sGRB, that would imply a possible afterglow signal in the LAT. These con-

siderations warrant the searches for counterparts for GW events on timescales typical of sGRB afterglows (few ks).

The standard LAT analysis assumes the source location to be known to some accuracy. Given the size of the localization region of the GW event, the search for a transient counterpart in LAT data is challenging and requires ad hoc methods. In the case of a non-detection, the measurement of an upper limit requires accounting for the uncertainty on the position of the source, that requires a careful statistical treatment. In this paper, we detail two methods to search for EM counterparts to GW events in *Fermi*-LAT data and to place upper limits in cases of non-detections. A comprehensive presentation of the results of the *Fermi*-LAT follow up for the three GW events using the methods presented here is provided in Ackermann et al. (2016) and Racusin et al. (2016).

2. Detection and localization of gravitational wave events by LIGO/VIRGO

Compact Binary Coalescence events discovered by the LIGO and VIRGO experiments (Abbott et al. 2016c, Abbott et al. 2016a) are localized with a Bayesian analysis that uses nested sampling to produced a marginalized posterior probability for the localization of the transient. This localization is distributed by the LIGO/VIRGO collaboration in the form of a full-sky map in HEALPix format (Górski et al. 2005), an equal-area projection, for which the value of each pixel p_h is the integral of the probability density over that pixel, so that

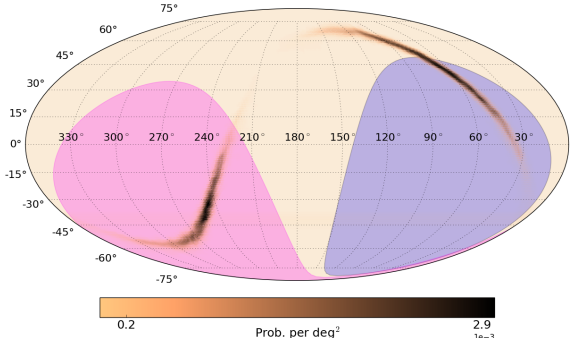


Fig. 1.— LIGO localization probability maps for LVT151012. The blue region represents the part of the sky occulted by the Earth at the trigger time from the vantage position of *Fermi*, ~ 560 km above the Earth surface. The pink region represents the LAT field of view at the time of the trigger (reproduced from Racusin et al. 2016).

$$\sum_{h=0}^H p_h = 1, \quad (1)$$

where H is the number of pixels.

We show in Fig. 1 one such map, provided by the LIGO collaboration for LVT151012 (Abbott et al. 2016a). The size of the 90% containment region for such a localization is usually of the order of several hundreds of square degrees. This will be reduced substantially as more GW detectors will come online. However, at the moment the search for a transient counterpart in such a large portion of the sky requires an ad-hoc treatment, described in the following sections.

3. Searching for EM counterparts to GW events in the *Fermi*-LAT data

Given the continuously-changing attitude of *Fermi*, a direction on the sky is typically observ-

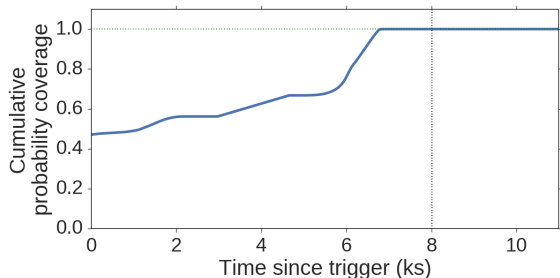


Fig. 2.— Cumulative sum of the probability of all the pixels observed within a given time since the trigger LVT151012 (see text for details). The vertical dashed line indicates the end of the time window used for the fixed time window analysis.

able by the LAT only for a given amount of time before it leaves the LAT FoV or is occulted by the Earth, to enter again after some time that depends on its position on the sky. Moreover, since the effective area of the LAT depends on the off-axis angle, the sensitivity of the LAT to a given sky position depends on the particular path that point takes in instrumental coordinates during the time window chosen for the analysis. It also depends on the astrophysical background at that position, that varies across the sky and is maximal for regions overlapping with the Galactic plane. Briefly, the Galactic plane is a significant background to sources in the LAT data due to the interaction of cosmic rays with the diffuse gas and the interstellar radiation field of the Milky Way. For this analysis, a direction in the sky is considered observable by the LAT if it is within 65° of the LAT boresight (or LAT z-axis) and has an angle with respect to the local zenith smaller than 100° . The latter requirement is used to exclude contamination from terrestrial γ rays produced by interactions of cosmic rays with the Earth’s atmosphere.

Given a probability map from LIGO (Fig-

ure 1), we define the cumulative coverage (*coverage* in the following) at a given time from the trigger t as the sum of the probabilities of all the pixels that have been observed by the LAT in the time window $[0, t]$:

$$C(t) = \sum_{h=0}^H p_h w_h(t), \quad (2)$$

where $h = 0 \dots H$ are the **HEALPix** pixels, and w_h is 1 if the h -th pixel has been observed by the LAT between the trigger time and t , and 0 otherwise. An example is shown in Fig. 2 for LVT151012: the LAT was covering a region amounting to $\sim 50\%$ of the total probability at the trigger time, and covered all the probability within ~ 7 ks. We use the plot of $C(t)$ to decide the time window for the fixed time window search described in the next section.

All of our analyses are based on the standard unbinned maximum likelihood technique used for LAT data analysis¹. We include in our *baseline* likelihood model all sources (point-like and extended) from the LAT source catalog (3FGL, Acero et al. 2015), as well as the Galactic and isotropic diffuse templates provided by the *Fermi*-LAT Collaboration (Acero et al. 2016). When needed, we employ a likelihood-ratio test (Neyman & Pearson 1928) to quantify whether the existence of a new source is statistically warranted. In doing so, we form a test statistic (TS) that is twice the logarithm of the ratio of the likelihood evaluated at the best-fit model parameters when including a candidate point source at a given position (alternative hypothesis) to the likelihood evaluated at the best-fit parameters under the baseline model (null

¹<http://fermi.gsfc.nasa.gov/ssc/data/analysis/documentation/Cicerone>

hypothesis). For all the likelihood analyses described in the next sections, we use the Pass 8 `P8_TRANSIENT010E_V6` event class and the corresponding instrument response functions.

In Sections 3.1 and 3.2, we describe the two techniques we developed to search for EM counterparts to GW events and to place upper limits on them. In Section 3.4, we comment on the use case for the resulting different sets of upper limits.

3.1. Fixed time window search

In this analysis we search for high-energy γ -ray emission on a fixed time window that starts at the time of the LIGO trigger. An obvious choice for this time window is the shortest time interval with total coverage, according to the definition given in the previous section. For example, in the case of LVT151012, we choose $T_{\text{fix}} = 0\text{--}8$ ks from the trigger time (see Fig. 2). Note that this is ~ 1 ks longer than the exact time at which the coverage is equal to 1 in order to accrue some exposure in the regions of the sky that were covered last.

We start by selecting all pixels that were observable by the LAT during T_{fix} and within the 90% containment of the LIGO localization maps, down-scaled to a resolution that matches the LAT Point Spread Function (PSF) at 100 MeV ($\sim 4^\circ$; $n_{\text{side}} = 128$). We then perform an independent likelihood analysis for each pixel, where we test for the presence of a new source at the center of the pixel. More specifically, for each pixel we consider a circular Region of Interest (RoI) with a radius of 8° placed at the center of the pixel, and we consider all events detected during T_{fix} above 100 MeV. We then perform a standard unbinned likelihood analysis

as described above. At the end, we take the maximum of TS over all the RoIs (TS_{max}). If TS_{max} is larger than 25, corresponding to $\sim 5 \sigma$ pre-trials, we proceed with computing the *post-trials* significance as described in Section 3.3. Otherwise we proceed with the computation of an upper limit as described in the next section.

3.1.1. Upper limit

If we do not find any new source according to the criteria described in the previous section, we proceed with the computation of an upper limit. We define the upper limit F_{ul} on the photon flux F of a source S in a Bayesian sense, as the upper boundary of a credibility interval starting at 0 and with a probability p_{ul} (Olive et al. 2014):

$$\int_0^{F_{ul}} P(F|D) dF = p_{ul}. \quad (3)$$

Here $P(F|D)$ represents the posterior probability for a flux of F given the data set D , marginalized over all the other parameters. Let us assume a power-law spectrum for the source S , with photon index α and photon flux F . We will compute upper limits in a narrow energy band; thus this assumption does not impact the results much (Ackermann et al. 2016). As explained above, the baseline model (background) is made up of the Galactic template, the isotropic template, and all sources from the 3FGL catalog. For simplicity, let us assume that this background model has no free parameters, i.e., we fix the normalization of the Galactic template and of the isotropic template to 1, and all the parameters for the 3FGL sources to their catalog values. We will relax this hypothesis later. Our likelihood model has then only 4 free parameters, namely α , F , and the longitude and lati-

tude pair $\vec{\delta}$ of S . The prior $\pi(\vec{\delta})$ on $\vec{\delta}$ is provided by the LIGO probability map. We use *uninformative* priors for the other parameters. We set a uniform prior $\pi(\alpha)$ between -10 and 10 for α . As suggested in the Review of Particle Physics (Olive et al. 2014), we used prior $\pi(F)$ for F uniform between a minimum of 0 and a maximum² of $100 \text{ photons cm}^{-2} \text{ s}^{-1}$ for F . The posterior probability marginalized with respect to α and $\vec{\delta}$ can be written as:

$$P(F|D) = \int \int P(\alpha, \vec{\delta}, F|D) d\alpha d\Omega, \quad (4)$$

where Ω represents solid angle. Bayes' theorem allows us to write:

$$P(\alpha, \vec{\delta}, F|D) \propto P(D|\alpha, \vec{\delta}, F) \pi(\alpha) \pi(\vec{\delta}) \pi(F), \quad (5)$$

where $P(D|\alpha, \vec{\delta}, F)$ is the likelihood function for our data set D . We have also assumed that the prior $\pi(\alpha, \vec{\delta}, F)$ can be written as $\pi(\alpha, \vec{\delta}, F) = \pi(\alpha) \pi(\vec{\delta}) \pi(F)$. In order to keep the marginalization computationally feasible, we substitute for the integration over the spatial dimension with a summation over the pixels of the LIGO map, adopting the following approximation:

$$\int P(D|\alpha, \vec{\delta}, F) \pi(\vec{\delta}) d\Omega \simeq \Omega \sum_{h=0}^H p_h P(D|\alpha, \vec{\delta}_h, F) \quad (6)$$

where p_h is the probability associated with the h -th pixel with center $\vec{\delta}_h$. We have also used the

²The particular value chosen as maximum does not influence the final results, as long as it is much higher than the flux of a realistic source. For comparison, the brightest source ever detected by the LAT was GRB 130427A, that reached a photon flux of a few $10^{-3} \text{ photons cm}^{-2} \text{ s}^{-1}$.

fact that **HEALPix** is an equal-area projection, and we have called Ω the solid angle covered by each pixel. We can now rewrite eq. 3 as:

$$\Omega \sum_{h=0}^H p_h \int_0^{F_{ul}} \int P(\alpha, \vec{\delta}_h, F|D) d\alpha dF = p_{ul}. \quad (7)$$

In other words, the upper limit F_{ul} is the value for which the following integral function:

$$U(x) = \Omega \sum_{h=0}^H p_h \int_0^x \int P(\alpha, \vec{\delta}_h, F|D) d\alpha dF \quad (8)$$

equals p_{ul} .

In order to compute this integral in practice we use a Markov Chain Monte Carlo (MCMC) technique. However, eq. 8 involves a likelihood function that considers the entire dataset D at once and is very expensive to compute. To reduce this complexity to a manageable level we start by observing that the MCMC can operate on the *un-normalized* posterior, that is, on the product of the likelihood function and the prior that we wrote in eq. 5. In this analysis we use the *unbinned* Poisson likelihood:

$$P(D|\alpha, \vec{\delta}_h, F) = \prod_{i=0}^N m_i(\alpha, \vec{\delta}_h, F) e^{-m_i(\alpha, \vec{\delta}_h, F)}, \quad (9)$$

where m_i is the photon density that the likelihood model yields at the energy and position of the i -th *event*³, and the product is performed over the *events* in our selection. In reality, the

³An *event* can be either a photon or a particle that has been mis-classified as a photon. Depending on the data class used in the analysis, the particle contamination can be more or less pronounced.

model prediction m_i does not depend on α or F for all events that are separated from $\vec{\delta}_h$ by more than the typical size of the LAT PSF. This observation is particularly true in our case since we are computing an upper limit, and the source is not detected because the flux F is below the LAT sensitivity. In other words, if we define $m_i(\alpha, \vec{\delta}_h, F) = m_{\text{bkg}} + m_{\text{src}}(\alpha, \vec{\delta}_h, F)$, the contribution from the source $m_{\text{src}} \sim 0$ if we are far enough from $\vec{\delta}_h$. Let us define an RoI centered on $\vec{\delta}_h$ and a radius big enough so that outside of the RoI $m_{\text{src}} \sim 0$. We can then write:

$$P(D|\alpha, \vec{\delta}_h, F) \propto \prod_{D_{\text{RoI}}} m_i(\alpha, \vec{\delta}_h, F) e^{-m_i(\alpha, \vec{\delta}_h, F)}, \quad (10)$$

where here the product is performed only over the events within our RoI (D_{RoI}). We can now write Bayes' theorem for one RoI as:

$$P(\alpha, \vec{\delta}_h, F|D) \propto P(D_{\text{RoI}}|\alpha, \vec{\delta}_h, F) \pi(\alpha) \pi(F) \quad (11)$$

This consideration allows us to compute the integral in eq. 8 by collecting separately (and in parallel) n_s samples from each RoI centered around each of the $\vec{\delta}_h$, and then merging these samples in one set weighted according to the probability of the corresponding pixel p_h . We can then base our inference on this merged set as representative of the full posterior probability.

In order to account for systematic uncertainties in the background model we also introduce two more parameters for each RoI, i.e., the normalizations of the isotropic template I and of the Galactic template G . We use a uniform prior $\pi(I)$ between 0 and 100 for I . For G instead we adopt a Gaussian prior with average 1 and standard deviation 0.15, as a conservative estimate of our systematic uncertainty. Since we introduce these two parameters in each one of the

n_{RoI} RoIs separately, they amount to $2 \times n_{\text{RoI}}$ nuisance parameters that are marginalized out in the final posterior. This allows us to take into account likely differences in systematic errors for different regions of the sky.

In practice, for each RoI we collect $n_s = 50,000$ samples $\vec{q}_s = (\alpha_s, F_s, I_s, G_s)$, with $s = 1..n_s$ using the sampler *emcee*⁴ (Foreman-Mackey et al. 2013). For each sample, we also compute the corresponding *energy* flux f_s by integrating the power-law with parameters F_s, α_s . We then estimate the integral of the marginalized posterior distribution for F and f by building the integral distribution of the F_s and the f_s and then using interpolation to obtain $u_h(x) = \int_0^x \int P(\vec{q}, \vec{\delta}_h, F|D) d\vec{q} dF$ (or the equivalent for f). The number of pixels outside of the 90% containment is much greater than within it but they do not contribute significantly to the probability (the sum of their probabilities is 0.1 by definition). Since considering all pixels would be computationally prohibitive, we instead assume that they have on average a posterior similar to the average of the pixels within the 90% containment. This is a reasonable assumption because even if the exposure of the LAT over the considered time scales is not perfectly uniform, all these points have low probabilities, so that any local variation is smoothed out. We have then $U(x) = \sum_{h=0}^H p_h u(x)$.

In principle the function $U(x)$ can be used to estimate the upper limit for any probability p_{ul} . However, the posterior is completely deter-

⁴The use of more powerful samplers such as MultiNest (Feroz et al. 2009) is unnecessary in this case, because we have only 4 parameters and we have verified that the posterior is not multimodal. Moreover, we are not interested in the Bayes' factor that cannot be directly computed given our approximations.

mined by the choice of the prior for F when F is small, i.e., the prior is no longer “uninformative”. Indeed, as F becomes smaller and smaller, the predicted number of counts from the source is ~ 0 and the likelihood becomes constant and independent of F and α . For this reason, p_{ul} should be chosen so that the data contain information about the corresponding flux level. As an example, we report in Figure 3 the posterior probability for the energy flux in the 0.1 – 1 GeV energy range for LVT151012. The flux level at which the blue curve in the right panel intersects a given probability $p_{ul} = P(< F)$ corresponds to the upper limit at that credibility level. In the left panel we can see that the posterior probability clearly deviates from a flat curve much earlier than the fluxes corresponding to the 90%, 95% and 99% credibility levels. This means that the likelihood function dominates over the prior at those fluxes.

3.2. Adaptive time window search

As in the previous analysis we perform an independent likelihood analysis for each pixel in the LIGO map, where we test for the presence of a new source at the center of the pixel. However, for this analysis we optimize separately the time window for each pixel. We define 8° radius RoIs centered at the center of each pixel. For the h -th pixel we define the interval T_h^{ad} that starts when the center \vec{p}_h of the ROI becomes observable by the LAT, i.e., when it is $< 65^\circ$ from the LAT boresight and $< 92^\circ$ from the local zenith, and ends when the \vec{p}_h is no longer observable⁵. First we measure the maximum test-statistic value ob-

tained among all the RoIs (TS_{max}). If TS_{max} is above our pre-trials threshold of 25, then we use the procedure described in Section 3.3 to compute its post-trials significance. If we do not find any significant excess, we compute a flux upper limit for each pixel separately with the semi-Bayesian technique (Helene 1983) implemented in the *Fermi ScienceTools*.

Figure 4 shows an example of the results returned by this analysis for LVT151012. We note that in this analysis the value of each upper limit is only relevant for the location of the corresponding pixel in the sky and the corresponding time interval. Therefore, for each upper limit separately the number of trials is $n_{\text{trials}} = 1$ and the confidence level of the upper limit (95% in the case shown in Fig. 4) does not need corrections. See Section 3.4 for specific-use cases for these different upper limits.

3.3. Detection threshold and trial factor

In a LAT analysis we normally choose to reject the null hypothesis (i.e., we deem a new source detected) when TS is greater than 25, roughly equivalent to a 5σ rejection criterion as confirmed by Monte Carlo simulations. In both analyses presented in the previous sections, however, we are considering multiple RoIs and testing for the presence of a source at different locations. Thus, the probability associated with the maximum test-statistic value found among all the RoIs (TS_{max}) must be corrected for an unknown trial factor n_{trials} . This is not simply the number of RoIs as the different regions overlap significantly. Moreover, n_{trials} depends on the angular size of the LIGO localization map and it is therefore different for different GW triggers. In principle one could estimate n_{trials}

⁵Note that, considering that the size of the RoI is 8° , the 92° zenith cut is equivalent to requiring that every point of the RoI has a zenith $\leq 100^\circ$.

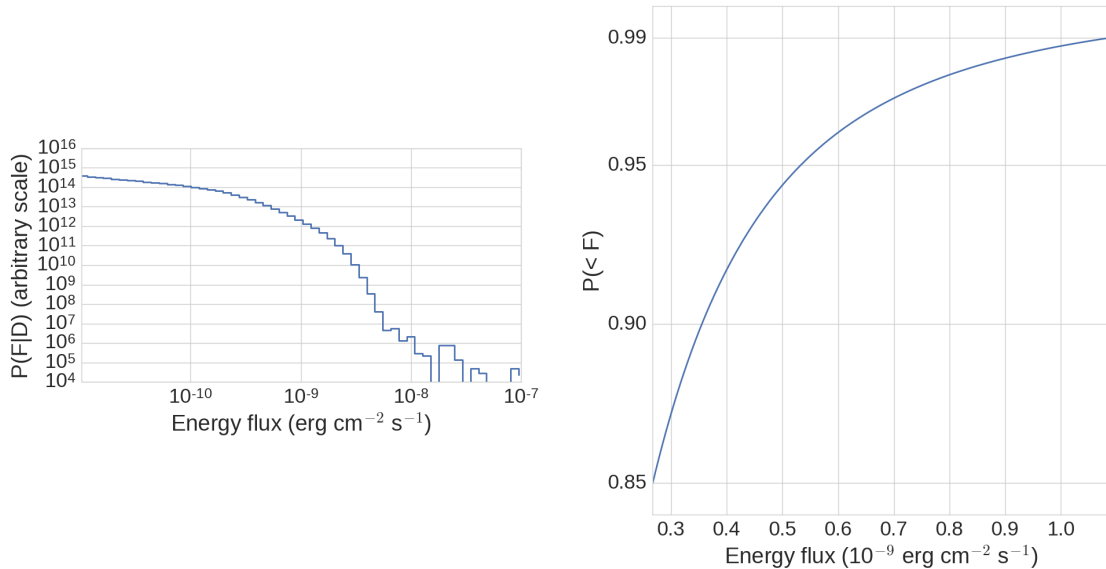


Fig. 3.— Differential (left) and integral (right) marginalized posterior for the 0.1–1 GeV energy flux for LVT151012 and the time window 0–8 ks. In the left panel, we note that the rightmost part of the distribution is affected by sampling noise. In the right panel (reproduced from Racusin et al. 2016), the flux at which the blue curve intersects a given probability $P(F < x)$ corresponds to the upper limit at that credibility level.

by repeating many times the same analysis on Monte Carlo realizations of the null hypothesis and directly measuring the probability of obtaining a test-statistic value that is at least as extreme as the one observed. However, this is not feasible in our case given the computational resources required for a single analysis. Instead, we adopt the method described in Vitells & Gross (2011) that allows an estimate of n_{trials} with just a few (~ 10) simulations. This procedure is manageable, but still time consuming. Since the trial factor always lowers the *post-trials* significance, we perform this computation only if we find $TS_{\text{max}} > 25$.

The procedure we just detailed requires for the null hypothesis to be a good representation of the case with no source, and that our Monte Carlo procedure faithfully simulates a

real observation. To verify this, we compared the distribution of observed test-statistic values in one instance of our analysis for LVT151012 with the expected distribution obtained from a Monte Carlo simulation. We generated a full-sky simulation using the `gtobssim` tool. The sky model consists of our null hypothesis, i.e., the Galactic emission template (we used the standard Galactic template `gll_iem_v06.fits`), the isotropic diffuse emission (tabulated in the `iso_P8R2_TRANSIENT010E_V6_v06.txt`) and all the sources from the 3FGL catalog (Acero et al. 2015). The actual pointing history of the satellite during the LIGO event was used so that the correct exposure of the sky was automatically taken into account. Then, we repeated the adaptive time window search on the simulated data. In Figure 5 we compare the TS distribu-

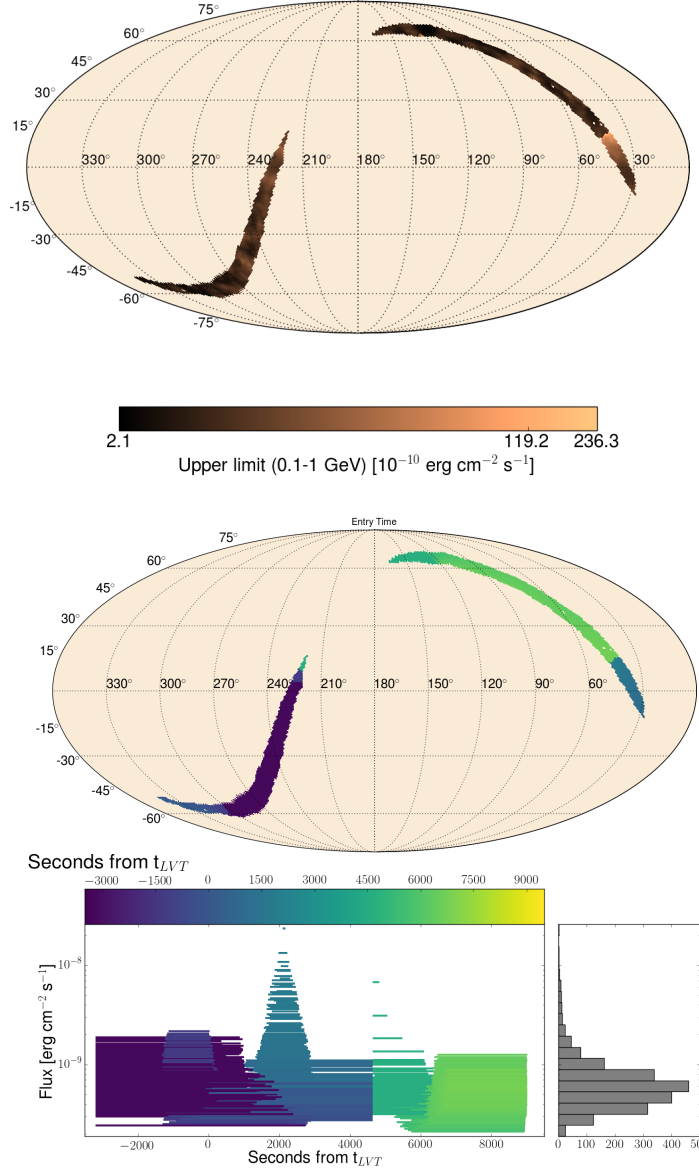


Fig. 4.— The adaptive time interval analysis for LVT151012 over the first *Fermi* orbit containing t_{LVT} : flux upper limit map during T_h^{ad} (*top*), the start time for T_h^{ad} relative to t_{LVT} for each pixel (*middle*), and the upper limit with the corresponding time window for each RoI (*bottom*). The vertical position in the bottom plot corresponds to the value of the LAT upper limit, and the horizontal line marks T_h^{ad} . The color of each line indicates the time when the RoI entered the LAT FoV, and matches exactly the color of the pixel in the middle panel. The horizontal histogram displays the distribution of the upper limits. Reproduced from Racusin et al. (2016).

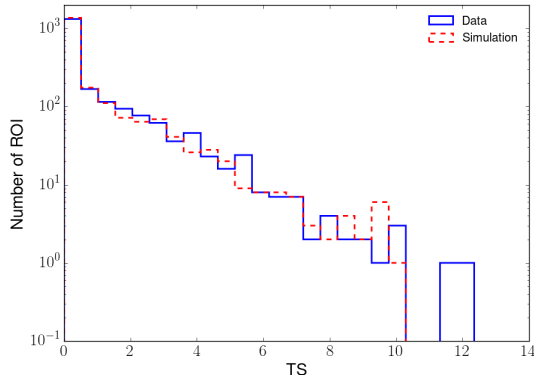


Fig. 5.— Comparison between the TS distributions of the data (solid blue histogram) and Monte Carlo simulations (dashed red curve).

tion obtained from flight data (filled line) and Monte Carlo (dashed line) for LVT151012. The distribution obtained from simulated data is a good match to the distribution of the TS values obtained from real data, and the good absolute agreement confirms that the model used in the simulation is a good representation of the sky and that the systematics of the analysis are well under control. As a result, our simulation procedure is suitable for computing the distribution of TS under the null hypothesis that no transient signal is present.

3.4. How to interpret LAT upper limits

In the previous sections we described the analyses to measure two different sets of upper limits. The upper limit produced by the fixed time window search (Section 3.1) is computed for time intervals during which the LAT covers a large part of the LIGO probability map. The analysis uses this map as a prior on the position of the counterpart. This upper limit applies in general to any model that predicts γ -ray

counterparts to GW events. The upper limits produced by the adaptive time window search (Section 3.2), instead, is computed for a time window T_h^{ad} that is different for each h -th pixel in the map. These limits are useful if more accurate information on the localization of a possible counterpart, for example from its detection by some other instrument, becomes available after the analysis has been performed and published. In this case, depending on the position of such a localization, the reader can choose the upper limit most relevant for the candidate counterpart *a posteriori*. Because the time windows have been optimized for each pixel, the corresponding upper limits could be deeper and hence more constraining with respect to the fixed time window analysis.

4. Discussion

With its wide FoV and its survey capabilities, *Fermi*-LAT is suitable for looking for EM counterparts to GW events above 100 MeV and for setting upper limits. In particular, in cases of NS-NS or NS-BH mergers, the expected EM counterpart is an sGRB. The LAT is a wide-field instrument that routinely detects and localizes GRBs during their afterglow phase. If the position measured by other instruments such as *Fermi*-GBM during the prompt phase has an uncertainty too large for follow up by X-ray, optical and radio telescopes, a LAT detection and localization can vastly improve the chances for a successful follow up. Moreover, the LAT is one of few instruments that can measure upper limits on the flux from the EM counterpart despite a large uncertainty on its position.

We have presented two novel techniques to perform the search for an EM counterpart to

a GW event in *Fermi*-LAT data and to provide upper limits. They fully exploit at the same time the capabilities of the instrument as well as the prior information available from the LIGO/VIRGO observatories. These methods, developed during the first LIGO science run ‘O1’, will be systematically used to search for EM counterparts to future GW events. In case of a detection, the methods presented here will return a localization, a flux estimation and a significance of the EM counterpart. If no EM counterpart is detected, a statistically meaningful set of upper limits can be measured.

The authors thank A. Strong (Max-Planck institute), J. Conrad (Stockholm University) and N.M. Mazziotta (INFN) for the helpful discussion on the STAT mailing list of the *Fermi*-LAT collaboration.

Some of the results in this paper have been derived using the HEALPix (Górski et al. 2005) package

The *Fermi*-LAT Collaboration acknowledges generous ongoing support from a number of agencies and institutes that have supported both the development and the operation of the LAT as well as scientific data analysis. These include the National Aeronautics and Space Administration and the Department of Energy in the United States, the Commissariat à l’Energie Atomique and the Centre National de la Recherche Scientifique / Institut National de Physique Nucléaire et de Physique des Particules in France, the Agenzia Spaziale Italiana and the Istituto Nazionale di Fisica Nucleare in Italy, the Ministry of Education, Culture, Sports, Science and Technology (MEXT), High Energy Accelerator Research Organization (KEK) and Japan Aerospace Exploration Agency (JAXA) in Japan, and the K. A. Wallenberg Foundation,

the Swedish Research Council and the Swedish National Space Board in Sweden.

Additional support for science analysis during the operations phase is gratefully acknowledged from the Istituto Nazionale di Astrofisica in Italy and the Centre National d’Études Spatiales in France.

REFERENCES

- Abramovici, A., Althouse, W. E., Drever, R. W. P., et al. 1992, *Science*, 256, 325
- Abbott, B. P., Abbott, R., Abbott, T. D., et al. 2016a, *Physical Review Letters*, 116, 241103
- Abbott, B. P., Abbott, R., Adhikari, R., et al. 2009, *Phys. Rev. D*, 80, 102001
- Abbott, B. P., Abbott, R., Abbott, T. D., et al. 2016b, *ArXiv e-prints*, arXiv:1602.08492 [astro-ph.HE]
- . 2016c, *Physical Review Letters*, 116, 061102
- Abeysekara, A. U., Aguilar, J. A., Aguilar, S., et al. 2012, *Astroparticle Physics*, 35, 641
- Acero, F., Ackermann, M., Ajello, M., et al. 2015, *ApJS*, 218, 23
- . 2016, *ApJS*, 223, 26
- Ackermann, M., Ajello, M., Asano, K., et al. 2013, *ApJ*, 763, 71
- Ackermann, M., Ajello, M., Albert, A., et al. 2016, *ApJ*, 823, L2
- Atwood, W. B., Abdo, A. A., Ackermann, M., et al. 2009, *ApJ*, 697, 1071

- Barthelmy, S. D., Barbier, L. M., Cummings, J. R., et al. 2005, *Space Sci. Rev.*, 120, 143
- Connaughton, V., Burns, E., Goldstein, A., et al. 2016, [arXiv:1602.03920 \[astro-ph.HE\]](#)
- De Pasquale, M., Schady, P., Kuin, N. P. M., et al. 2010, *ApJ*, 709, L146
- Dirirsa, F., Racusin, J., McEnery, E., & Desiante, R. 2016, GRB Coordinates Network, 19580
- Eichler, D., Livio, M., Piran, T., & Schramm, D. N. 1989, *Nature*, 340, 126
- Feroz, F., Hobson, M. P., & Bridges, M. 2009, *MNRAS*, 398, 1601
- Foreman-Mackey, D., Hogg, D. W., Lang, D., & Goodman, J. 2013, *PASP*, 125, 306
- Fraschetti, F. 2016, *ArXiv e-prints*, [arXiv:1603.01950 \[astro-ph.HE\]](#)
- Ghirlanda, G., Salvaterra, R., Campana, S., et al. 2015, *A&A*, 578, A71
- Górski, K. M., Hivon, E., Banday, A. J., et al. 2005, *ApJ*, 622, 759
- Greiner, J., Burgess, J. M., Savchenko, V., & Yu, H.-F. 2016, *ArXiv e-prints*, [arXiv:1606.00314 \[astro-ph.HE\]](#)
- Helene, O. 1983, *Nuclear Instruments and Methods in Physics Research*, 212, 319
- Janiuk, A., Bejger, M., Charzynski, S., & Sukova, P. 2016, *A&A*, submitted, [arXiv:1604.07132 \[astro-ph.HE\]](#)
- Kouveliotou, C., Granot, J., Racusin, J. L., et al. 2013, *ApJ*, 779, L1
- Lee, W. H., & Ramirez-Ruiz, E. 2007, *New Journal of Physics*, 9, 17
- Lipunov, V. M., Gorosabel, J., Pruzhinskaya, M. V., et al. 2016, *MNRAS*, 455, 712
- Loeb, A. 2016, *ApJ*, 819, L21
- Longo, F., Bissaldi, E., Bregeon, J., et al. 2016, GRB Coordinates Network, 19403
- Lyutikov, M. 2016, *ArXiv e-prints*, [arXiv:1602.07352 \[astro-ph.HE\]](#)
- Meegan, C., Lichti, G., Bhat, P. N., et al. 2009, *ApJ*, 702, 791
- Mereghetti, S., Götz, D., Borkowski, J., Walter, R., & Pedersen, H. 2003, *A&A*, 411, L291
- Nakar, E. 2007, *Phys. Rep.*, 442, 166
- Narayan, R., Paczynski, B., & Piran, T. 1992, *ApJ*, 395, L83
- Neyman, J., & Pearson, E. S. 1928, *Biometrika*, 20, 175
- Ohno, M., & Pelassa, V. 2009, GRB Coordinates Network, 9334
- Olive, K. A., et al. 2014, *Chin. Phys.*, C38, 090001
- Perna, R., Lazzati, D., & Giacomazzo, B. 2016, *ApJ*, 821, L18
- Racusin, J. L., Zhu, S., Kocevski, D., et al. 2013, GRB Coordinates Network, 15464
- Racusin, J. L., Burns, E., Goldstein, A., et al. 2016, *ArXiv e-prints*, [arXiv:1606.04901 \[astro-ph.HE\]](#)
- Savchenko, V., Ferrigno, C., Mereghetti, S., et al. 2016, *ApJ*, 820, L36

Singer, L. P., Kasliwal, M. M., Cenko, S. B.,
et al. 2015, ApJ, 806, 52

Vianello, G., Omodei, N., & Fermi/LAT
collaboration. 2015, ArXiv e-prints,
arXiv:1502.03122 [astro-ph.HE]

Vitells, O., & Gross, E. 2011, Astroparticle
Physics, 35, 230